

Observation of a thermoelectric Hall plateau in the extreme quantum limit

Wenjie Zhang^{1,*}, Peipei Wang^{2,*}, Brian Skinner^{3,4,*}, Ran Bi¹, Vladyslav Kozii^{3,5,6}, Chang-Woo Cho², Ruidan Zhong⁷, John Schneeloch⁷, Dapeng Yu², Genda Gu⁷, Liang Fu^{3,†}, Xiaosong Wu^{1,8,†}, Liyuan Zhang^{2,†}

¹State Key Laboratory for Artificial Microstructure and Mesoscopic Physics, Beijing Key Laboratory of Quantum Devices, Peking University, Beijing 100871, China

²Department of Physics, Southern University of Science and Technology, Shenzhen 518055, China

³ Department of Physics, Massachusetts Institute of Technology, Cambridge, MA 02139, USA

⁴ Department of Physics, Ohio State University, Columbus, OH 43210, USA

⁵ Department of Physics, University of California, Berkeley, CA 94720, USA

⁶ Materials Sciences Division, Lawrence Berkeley National Laboratory, Berkeley, CA 94720, USA

⁷ Condensed Matter Physics and Materials Science Department, Brookhaven National Laboratory, Upton, New York 11973, USA

⁸ Frontiers Science Center for Nano-optoelectronics and Collaborative Innovation Center of Quantum Matter, Peking University, Beijing 100871, China

*These authors contributed equally.

†Corresponding Author. E-mail: liangfu@mit.edu (L.F.), xswu@pku.edu.cn (X.W.), zhangly@sustech.edu.cn (L.Z.)

The thermoelectric Hall effect is the generation of a transverse heat current upon applying an electric field in the presence of a magnetic field. Here we demonstrate that the thermoelectric Hall conductivity α_{xy} in the three-dimensional Dirac semimetal ZrTe_5 acquires a robust plateau in the extreme quantum limit

of magnetic field. The plateau value is independent of the field strength, disorder strength, carrier concentration, or carrier sign. We explain this plateau theoretically and show that it is a unique signature of three-dimensional Dirac or Weyl electrons in the extreme quantum limit. We further find that other thermoelectric coefficients, such as the thermopower and Nernst coefficient, are greatly enhanced over their zero-field values even at relatively low fields.

1 Introduction

Dirac materials offer the promise of uncommonly robust transport properties. For example, two-dimensional graphene exhibits an optical absorption that is a universal constant over a wide range of frequencies [1, 2, 3], and three-dimensional (3D) Dirac materials can display enormous electrical mobility [4] and photogalvanic response [5, 6]. These capabilities of Dirac materials arise from their occupying a classification intermediate between the conventional dichotomy of metals and insulators: like insulators, Dirac materials have vanishing carrier density and density of states when not doped, and, like metals, they have no energy gap to electrical and thermal excitations.

This combination of properties becomes especially tantalizing when applied to the thermoelectric effect, which is the generation of electrical voltage from a temperature gradient. A recent theoretical study suggested that the thermoelectric Hall conductivity in three-dimensional Dirac or Weyl semimetals acquires a universal plateau value at sufficiently large magnetic fields [7]. This value is independent of disorder, carrier concentration, or magnetic field, and leads to the unbounded growth of the thermopower and the thermoelectric figure of merit with increasing field [8]. These findings imply a potential pathway for achieving efficient platforms for waste heat recovery or solid state refrigeration [9].

In this work we report on the observation of a robust plateau in the thermoelectric Hall con-

ductivity α_{xy} in strong magnetic fields in the Dirac semimetal ZrTe_5 . The measured value of α_{xy} agrees well with the theoretical predictions. Furthermore, we observe a highly sensitive field dependence of the thermoelectric responses — including α_{xy} , the thermopower S_{xx} , and the Nernst coefficient S_{xy} — at $T \approx 90\text{K}$, leading to enormous enhancement of the thermoelectric properties at relatively low fields $\leq 1\text{ T}$, which can even be achieved by permanent magnets.

2 Results

2.1 Electron bands in ZrTe_5

Our observation of the plateau in the thermoelectric Hall conductivity and the rapid growth of the thermopower in ZrTe_5 is enabled by two key factors. First, the material is metallic with an ultralow electron concentration, which allows the system to reach the extreme quantum limit (EQL) of magnetic field already at $B \approx 1\text{ T}$. Second, the high mobility of our samples, $\mu \approx 640,000\text{ cm}^2/\text{Vs}$, implies that the system reaches the dissipationless limit for electron transport already at $B \approx 0.1\text{ T}$. Taken together, these factors allow us to observe the robust thermoelectric Hall response in the EQL, as well as significant enhancement of thermoelectric properties at low fields.

In terms of its electronic properties, bulk ZrTe_5 lies somewhere between a strong topological insulator and a weak one, depending sensitively on the crystal lattice constant. [10] At this phase boundary the band structure realizes a gapless Dirac dispersion around the Γ point. Because of the sensitivity of the band structure, indications of all three phases have been reported by various groups [11, 12, 13, 14, 15, 16, 17]. There seems to be a consensus that the band structure depends on the growth method, defect concentration, or thickness of the sample [18, 19, 20, 21]. Our 3D bulk samples, grown by the tellurium flux method at Brookhaven National Laboratory, have been consistently found to be 3D Dirac semimetals with no gap, or at most a very small gap below detection limits, in multiple studies by different techniques,

such as ARPES, magneto-optical spectroscopy and transport [11, 12, 13, 14, 15, 17, 22]. Interestingly, a gap of 10 meV develops when the thickness of the sample is reduced to 180 nm, further confirming the sensitivity [18]. Since ZrTe₅ grown under certain conditions possesses a single Dirac cone and can be grown with very low carrier concentration and very high mobility, it represents an ideal platform for studying fundamental properties and possible applications of 3D Dirac electrons both in weak and strong magnetic fields. The possibility of a small band gap, and its influence on the thermoelectric Hall conductivity, are discussed in more detail in Supplementary Note 6.

2.2 Temperature and magnetic field dependence of resistivity

The electron concentration in our samples, as measured by the Hall effect, is $n_{\text{Hall}} \approx 5 \times 10^{16} \text{ cm}^{-3}$ at low temperature. As we show below, at such low densities the EQL is reached already at fields $\gtrsim 2 \text{ T}$. The Hall effect remains linear in the magnetic field B up to 6 T at low temperatures, which is much higher than the quantum limit field. This linearity reflects a single band of carriers, indicating that we have a simple Dirac system. As in previous studies of ZrTe₅ [17, 23], the Hall concentration n_{Hall} is seen to evolve with both temperature and magnetic field, with the sample changing from n -type to p -type as T is increased above $\approx 83 \text{ K}$. Previous studies suggest that this change results from a temperature-dependent Lifshitz transition [22, 23]; a more thorough discussion of the electron and hole concentrations as a function of temperature is presented in Supplementary Note 2. Since the sign of the thermopower S_{xx} is determined by the carrier type, i.e., positive for holes and negative for electrons, the shift from n -type to p -type transport with increasing temperature is also reflected in the temperature dependence of S_{xx} , which reverses its sign at $T \approx 90 \text{ K}$, as shown in Fig. 1c [24]. At the critical temperature where the carrier density is the lowest, the resistivity is at its maximum.

As the magnetic field is increased from zero, the resistivity undergoes Shubnikov-de Haas

(SdH) oscillations associated with depopulation of high Landau levels. These oscillations are plotted in Fig. 1b, which show that the EQL is achieved at all fields > 2 T. The appearance of SdH oscillations at very low field (≈ 0.1 T) reflects the high mobility of our samples, $\mu \approx 640,000 \text{ cm}^2\text{V}^{-1}\text{s}^{-1}$. A previous study reported measurements of the SdH oscillations for the magnetic field oriented along the x , y and z axes, from which the Fermi surface morphology is obtained [17]. The Fermi surface is an ellipsoid with the longest principal axis in the z direction. The carrier density estimated from SdH oscillations is in good agreement with n_{Hall} , confirming the dominance of a single band at the Fermi level at low temperature. The corresponding Fermi level is only 11 meV above the Dirac point at $T = 1.5$ K.

2.3 Thermoelectric coefficients in the extreme quantum limit

Because of the low carrier density, the system enters the lowest ($N = 0$) Landau level at $B > 2$ T at low temperature. As the temperature is increased, the Fermi level shifts towards the Dirac point, implying that the quantum limit is reached at an even lower field. Therefore, the system is well within the EQL for a large range of magnetic field, which we sweep up to 14 T.

Our measurements of the longitudinal (Seebeck, S_{xx}) and transverse (Nernst, S_{xy}) thermoelectric coefficients are shown in Fig. 2 as a function of magnetic field. There is a general increase in the magnitude of both S_{xx} and S_{xy} with magnetic field in the EQL. Indeed, at $T \approx 90$ K, where the carrier density is the lowest, S_{xx} becomes as large as $800 \mu\text{V/K}$, while S_{xy} becomes larger than $1200 \mu\text{V/K}$. The theoretical interpretation of S_{xx} and S_{xy} , however, is complicated by the variation of the carrier density with T and B . Indeed, the change in sign of S_{xx} with B at higher temperatures is likely related to the proximity of the system to a transition from n -type to p -type conduction (as mentioned above), as is the sharp variation in S_{xx} with B at low fields and $T \approx 90$ K. This variation of the carrier concentration with B seems to blunt the large, linear enhancement of S_{xx} with B predicted in Ref. [8] for higher temperatures.

(A similar shift in chemical potential with B field may be responsible for the nonmonotonic dependence of S_{xx} on B seen in an organic Dirac material [25].)

These complications lead us to examine a more fundamental quantity, the thermoelectric conductivity $\hat{\alpha} = \hat{\rho}^{-1}\hat{S}$. Here $\hat{\rho}$ and \hat{S} denote the resistivity and thermoelectric tensors, respectively, so that both the longitudinal and transverse components of the tensor $\hat{\alpha}$ can be deduced from our measurements. We focus, in particular, on the thermoelectric Hall conductivity α_{xy} , which is plotted in Fig. 3 for the EQL. While α_{xy} depends in general on both T and B , Fig. 3b shows that deep in the EQL α_{xy} achieves a plateau that is independent of magnetic field. Furthermore, this plateau value of α_{xy} is linear in temperature at temperatures $T \lesssim 100$ K, which suggests that α_{xy}/T is a constant in the EQL, independent of B or T (Fig. 3a, see also Supplementary Note 3).

3 Discussion

This strikingly universal value of α_{xy}/T can be understood using the following argument. The thermoelectric Hall conductivity can be defined by $\alpha_{xy} = J_y^Q/(TE_x)$, where J_y^Q is the heat current density in the y direction under conditions where an electric field E_x is applied in the x direction and the temperature T is uniform. In the limit of large magnetic field (large Hall angle), electrons drift perpendicular to the electric field via the $\vec{E} \times \vec{B}$ drift, and thus their flow is essentially dissipationless with a drift velocity $v_d = E_x/B$ in the y direction. The heat current density J_y^Q can be described by the law governing reversible processes, $J_y^Q = TJ_y^S$, where $J_y^S = v_d\mathcal{S}$ is the entropy current density and $\mathcal{S} = (\pi^2/3)k_B^2T\nu$ is the electronic entropy per unit volume, with ν the density of states [26]. Crucially, for a gapless Dirac system in the EQL, the density of states approaches an energy-independent constant, $\nu = N_f eB/(2\pi^2\hbar^2v_F)$, where \hbar is the reduced Planck constant, v_F is the Dirac velocity in the field direction, and N_f is an integer that counts the number of Dirac points, assuming that all Dirac points are degenerate

in energy. (In our system $N_f = 1$; for a Weyl system N_f is given by half the number of Weyl points.) Inserting this expression for ν into the relations for \mathcal{S} and α_{xy} gives

$$\alpha_{xy} = \frac{1}{6} \frac{T}{v_F} \frac{ek_B^2}{\hbar^2} N_f. \quad (1)$$

In other words, in the EQL the value of α_{xy}/T is determined only by the Dirac velocity, by the integer degeneracy factor N_f , and by fundamental constants of nature. In this sense one can say that $\alpha_{xy}v_F/T$ is a universal quantity in the EQL of Dirac or Weyl materials, which depends only on fundamental constants and on the integer N_f . Equation (1) was predicted in Ref. [7], where it was derived in terms of quantum Hall-like edge states.

Notice, in particular, that Eq. (1) has no dependence on the carrier concentration. Thus, changes in the carrier concentration or even a transition from n -type to p -type conduction do not affect the value of α_{xy} . Empirical evidence for this lack of dependence can be seen by noting that the carrier concentration and carrier sign vary strongly within the range of T and B corresponding to the plateau in α_{xy} (see Supplementary Note 2 for more discussion). The surprising independence of α_{xy} on the carrier concentration apparently enables the universal plateau that we observe in α_{xy} , even though the behavior of S_{xx} and S_{xy} in the EQL is more complicated. Figure 3a shows that the plateau in $\alpha_{xy}/T \approx 0.01 \text{ AK}^{-2}\text{m}^{-1}$. We can compare this to the theoretical prediction of Eq. (1) using the previously-measured Dirac velocity $v_F \approx 3 \times 10^4 \text{ m/s}$ [17]. Inserting this value into Eq. (1) gives $\alpha_{xy}/T \approx 0.015 \text{ AK}^{-2}\text{m}^{-1}$, which is in excellent agreement with our measurement. (Data from another sample is presented in Supplementary Note 4.) Equation (1) also predicts a lack of dependence on the disorder strength, in the sense that the value of α_{xy} has no dependence on the electron mobility or transport scattering time. This lack of dependence on disorder is more difficult to directly test experimentally.

It is worth emphasizing that in conventional gapped systems, such as doped semiconductors, α_{xy} varies with both the carrier concentration n and the magnetic field B in a nontrivial way [7].

In this sense the plateau in α_{xy}/T is a unique Hallmark of three-dimensional Dirac and Weyl semimetals. (The effects of a finite band gap on α_{xy} are discussed in Supplementary Note 6.)

Finally, we briefly comment on the possibility of making efficient thermoelectric devices using the strong magnetic field enhancement of the thermoelectric coefficients that we observe. In particular, the strong enhancement of the longitudinal and transverse thermoelectric coefficients, S_{xx} and S_{xy} , would seem to suggest a large enhancement of the thermoelectric power factor $\text{PF} = S_{xx}^2/\rho_{xx}$. Unfortunately, the growth in S_{xx} with field is compensated by the large magnetoresistance in ZrTe_5 (as we discuss in Supplementary Note 2), so that no significant growth of the power factor is seen. The variation in carrier density with magnetic field B also blunts the field enhancement of the thermopower, particularly at higher temperatures. Thus, direct use of ZrTe_5 in thermoelectric devices will likely require further research that can find a way to suppress the magnetoresistance while maintaining the large magnetothermoelectric effect.

In summary, in this article we have demonstrated a robust plateau in the thermoelectric Hall conductivity of Dirac or Weyl semimetals. This plateau is unique to three-dimensional Dirac or Weyl electrons, and gives rise to the large, field-enhanced thermoelectric response that we observe at strong magnetic field. Our findings imply that ZrTe_5 , and three-dimensional nodal semimetals more generally, may serve as effective platforms for achieving large thermopower and other unique thermoelectric responses. Our findings also suggest a transport probe for identifying and characterizing three-dimensional Dirac materials.

4 Methods

Our samples are single crystals of ZrTe_5 grown by the tellurium flux method [12, 14, 17, 22]. Relatively large crystals, with a typical size of $3 \text{ mm} \times 0.4 \text{ mm} \times 0.3 \text{ mm}$, were used for transport measurements. The longest dimension is along the a axis and the shortest dimension is

along the b axis. In our measurements, either the electrical current or the temperature gradient is applied along the a axis, while the magnetic field is perpendicular to the ac plane. For the thermoelectric measurements, one end of the sample is thermally anchored to the sample stage, while the other end is attached to a resistive heater (see Fig. 1b). The temperature difference between the two ends is measured by a type-E thermocouple. This difference is in the range of 100 to 160 mK, which is always much smaller than the sample temperature. (See Supplementary Note 1 for further details about our measurement setup.)

We use a two-point method to measure the temperature difference between the hot end and cold end of the sample. (The relative advantages of two-point and four-point setups for thermoelectric measurements are discussed in Supplementary Note 1). Two Type-E thermocouples are attached to the heater stage and the heat sink, respectively (see Supplementary Fig. 2). Thermoelectric voltages are measured through gold wires attached to two ends of the sample and the voltage probes in the middle. ρ_{xx} and ρ_{xy} are measured by a standard four-point method.

References

- [1] T. Ando, Y. Zheng, and H. Suzuura, Dynamical Conductivity and Zero-Mode Anomaly in Honeycomb Lattices, *J. Phys. Soc. Japan* **71**, 1318-1324 (2002).
- [2] V. P. Gusynin and S. G. Sharapov, Transport of Dirac quasiparticles in graphene: Hall and optical conductivities, *Phys. Rev. B* **73**, 245411 (2006).
- [3] K. F. Mak, M. T. Sfeir, Y. Wu, C. H. Lui, J. A. Misewich, and T. F. Heinz, Measurement of the optical conductivity of graphene, *Phys. Rev. Lett.* **101**, 196405 (2008).
- [4] Tian Liang, Quinn Gibson, Mazhar N. Ali, Minhao Liu, R. J. Cava, N. P. Ong, Ultrahigh mobility and giant magnetoresistance in the Dirac semimetal Cd_3As_2 , *Nat. Mat.* **14**, 280-284 (2015).

- [5] C.-K. Chan, N. H. Lindner, G. Refael, and P. A. Lee, Photocurrents in Weyl semimetals, *Phys. Rev. B* **95**, 041104(R) (2017).
- [6] F. de Juan, A. G. Grushin, T. Morimoto, and J. E. Moore, Quantized circular photogalvanic effect in Weyl semimetals, *Nat. Comm.* **8**, 15995 (2017).
- [7] Vladyslav Kozii, Brian Skinner, and Liang Fu, Thermoelectric Hall conductivity and figure of merit in Dirac/Weyl materials, *Phys. Rev. B* **99**, 155123 (2019).
- [8] Brian Skinner and Liang Fu, Large, nonsaturating thermopower in a quantizing magnetic field, *Sci. Adv.* **4**, 2621 (2018).
- [9] A. Shakouri, Recent developments in semiconductor thermoelectric physics and materials, *Annu. Rev. Mat. Res.* **41**, 399-431 (2011).
- [10] Hongming Weng, Xi Dai, and Zhong Fang, Transition-Metal Pentatelluride ZrTe_5 and HfTe_5 : A Paradigm for Large-Gap Quantum Spin Hall Insulators, *Phys. Rev. X* **4**, 011002 (2014).
- [11] G. Manzoni, A. Sterzi, A. Crepaldi, M. Diego, F. Cilento, M. Zacchigna, Ph. Bugnon, H. Berger, A. Magrez, M. Grioni, and F. Parmigiani Ultrafast Optical Control of the Electronic Properties of ZrTe_5 , *Phys. Rev. Lett.* **115**, 207402 (2015).
- [12] R. Y. Chen, S. J. Zhang, J. A. Schneeloch, C. Zhang, Q. Li, G. D. Gu, and N. L. Wang, Optical spectroscopy study of the three-dimensional Dirac semimetal ZrTe_5 , *Phys. Rev. B* **92**, 075107 (2015).
- [13] R. Y. Chen, Z. G. Chen, X.-Y. Song, J. A. Schneeloch, G. D. Gu, F. Wang, and N. L. Wang, Magnetoinfrared Spectroscopy of Landau Levels and Zeeman Splitting of

- Three-Dimensional Massless Dirac Fermions in ZrTe_5 , *Phys. Rev. Lett.* **115**, 176404 (2015).
- [14] Qiang Li, Dmitri E. Kharzeev, Cheng Zhang, Yuan Huang, I. Pletikosić, A. V. Fedorov, R. D. Zhong, J. A. Schneeloch, G. D. Gu, and T. Valla, Chiral magnetic effect in ZrTe_5 , *Nat. Phys.* **12**, 550-554 (2016).
- [15] Jingyue Wang, Jingjing Niu, Baoming Yan, Xinqi Li, Ran Bi, Yuan Yao, Dapeng Yu, and Xiaosong Wu, Vanishing quantum oscillations in Dirac semimetal ZrTe_5 , *PNAS* **115**, 9145-9150 (2018).
- [16] Xiang-Bing Li, Wen-Kai Huang, Yang-Yang Lv, Kai-Wen Zhang, Chao-Long Yang, Bin-Bin Zhang, Y. B. Chen, Shu-Hua Yao, Jian Zhou, Ming-Hui Lu, Li Sheng, Shao-Chun Li, Jin-Feng Jia, Qi-Kun Xue, Yan-Feng Chen, and Ding-Yu Xing, Experimental Observation of Topological Edge States at the Surface Step Edge of the Topological Insulator ZrTe_5 , *Phys. Rev. Lett.* **116**, 176803 (2016).
- [17] Fangdong Tang, Yafei Ren, Peipei Wang, Ruidan Zhong, J. Schneeloch, Shengyuan A. Yang, Kun Yang, Patrick A. Lee, Genda Gu, Zhenhua Qiao, and Liyuan Zhang, Three-dimensional quantum Hall effect and metal-insulator transition in ZrTe_5 , *Nature* **569**, 537-541 (2019).
- [18] Zhi-Guo Chen, R. Y. Chen, R. D. Zhong, John Schneeloch, C. Zhang, Y. Huang, Fanming Qu, Rui Yu, Q. Li, G. D. Gu, and N. L. Wang, Spectroscopic evidence for bulk-band inversion and three-dimensional massive Dirac fermions in ZrTe_5 , *PNAS* **114**, 816-821 (2017).

- [19] Jingjing Niu, Jingyue Wang, Zhijie He, Chenglong Zhang, Xinqi Li, Tuocheng Cai, Xi-umei Ma, Shuang Jia, Dapeng Yu, and Xiaosong Wu, Electrical transport in nanothick ZrTe_5 sheets: From three to two dimensions, *Phys. Rev. B* **95**, 035420 (2017).
- [20] Jianwei Lu, Guolin Zheng, Xiangde Zhu, Wei Ning, Hongwei Zhang, Jiyong Yang, Haifeng Du, Kun Yang, Haizhou Lu, Yuheng Zhang, and Mingliang Tian, Thickness-tuned transition of band topology in ZrTe_5 nanosheets, *Phys. Rev. B* **95**, 125135 (2017).
- [21] P. Shahi, D. J. Singh, J. P. Sun, L. X. Zhao, G. F. Chen, Y. Y. Lu, J. Li, J.-Q. Yan, D. G. Mandrus, and J.-G. Cheng, Bipolar Conduction as the Possible Origin of the Electronic Transition in Pentatellurides: Metallic vs Semiconducting Behavior, *Phys. Rev. X* **8**, 021055 (2018).
- [22] Hang Chi, Cheng Zhang, Genda Gu, Dmitri E Kharzeev, Xi Dai, and Qiang Li, Lifshitz transition mediated electronic transport anomaly in bulk ZrTe_5 , *N. J. Phys.* **19**, 015005 (2017).
- [23] Yan Zhang, Chenlu Wang, Li Yu, Guodong Liu, Aiji Liang, Jianwei Huang, Simin Nie, Xuan Sun, Yuxiao Zhang, Bing Shen, Jing Liu, Hongming Weng, Lingxiao Zhao, Genfu Chen, Xiaowen Jia, Cheng Hu, Ying Ding, Wenjuan Zhao, Qiang Gao, Cong Li, Shaolong He, Lin Zhao, Fengfeng Zhang, Shenjin Zhang, Feng Yang, Zhimin Wang, Qinjun Peng, Xi Dai, Zhong Fang, Zuyan Xu, Chuangtian Chen, and X. J. Zhou, Electronic evidence of temperature-induced Lifshitz transition and topological nature in ZrTe_5 , *Nat. Comm.* **8**, 15512 (2017).
- [24] T. M. Tritt and R. Littleton, “Thermoelectric properties of the transition metal pentatellurides: Potential low-temperature thermoelectric materials,” in *Recent Trends in Thermoelectric Materials Research II*, T. M. Tritt (ed.). Academic Press, 2001, Ch. 6, 179-206.

[25] T. Konoike, M. Sato, K. Uchida, and T. Osada, Anomalous Thermoelectric Transport and Giant Nernst Effect in Multilayered Massless Dirac Fermion System, *J. Phys. Soc. Jpn.* **82**, 073601 (2013).

[26] N. W. Ashcroft and N. D. Mermin, *Solid State Physics* (Holt, Rinehart and Winston, 1976).

Acknowledgments

Financial support for W.Z., R.B., and X.W. comes from the National Key Basic Research Program of China (No. 2016YFA0300600) and NSFC (No. 11574005, No. 11774009). Work at SUSTech was supported by Guangdong Innovative and Entrepreneurial Research Team Program (No. 2016ZT06D348), NFSC (11874193) and Shenzhen Fundamental subject research Program (JCYJ20170817110751776) and Innovation Commission of Shenzhen Municipality (Grant No. KQTD2016022619565991). Work at MIT was supported by DOE Office of Basic Energy Sciences, Division of Materials Sciences and Engineering under Award de-sc0018945. BS was supported by the NSF STC “Center for Integrated Quantum Materials” under Cooperative Agreement No. DMR-1231319. VK was supported by the Quantum Materials program at LBNL, funded by the US Department of Energy under Contract No. DE-AC02-05CH11231. Work at Brookhaven is supported by the Office of Basic Energy Sciences, U.S. Department of Energy under Contract No. de-sc0012704.

Author Contributions

LF, XW, and LZ conceived the idea for this study. WZ, PW, RB, CWC, XW, and LZ performed the measurements and analyzed the associated data. DY contributed to the discussion of the results. BS, VK, and LF provided theoretical analysis. RZ, JS, and GG grew the samples. BS, VK, XW, and LZ wrote the manuscript, with input from all authors.

Competing Interests

The authors declare no competing interests.

Data Availability

The data that support the findings of this study are available from the corresponding authors upon reasonable request.

Supplementary materials

Supplementary Text

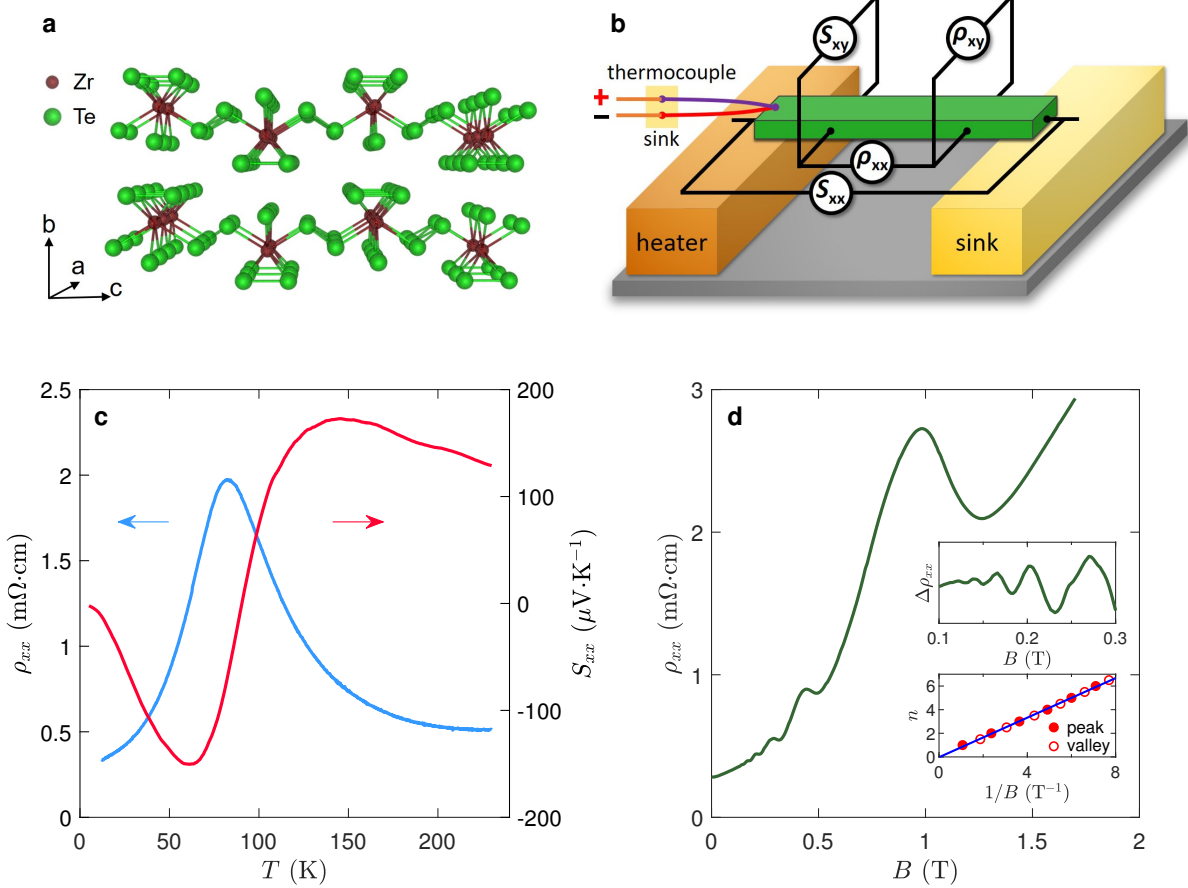


Figure 1: Measurement setup and resistivity. **a** The crystal structure of ZrTe_5 . **b** The measurement setup for resistivity and thermoelectric measurements. **c** Temperature dependence of the electrical resistivity (blue curve, left vertical axis) and the thermopower (red curve, right vertical axis). **d** Magnetoresistance at 1.5 K. On top of a strong positive magnetoresistance, SdH oscillations are evident (upper inset). The onset field of the oscillations is 0.13 T, indicating a high mobility. The system enters the EQL at ≈ 2 T. The lower inset shows the index n of the minima and maxima of each oscillation as a function of $1/B$.

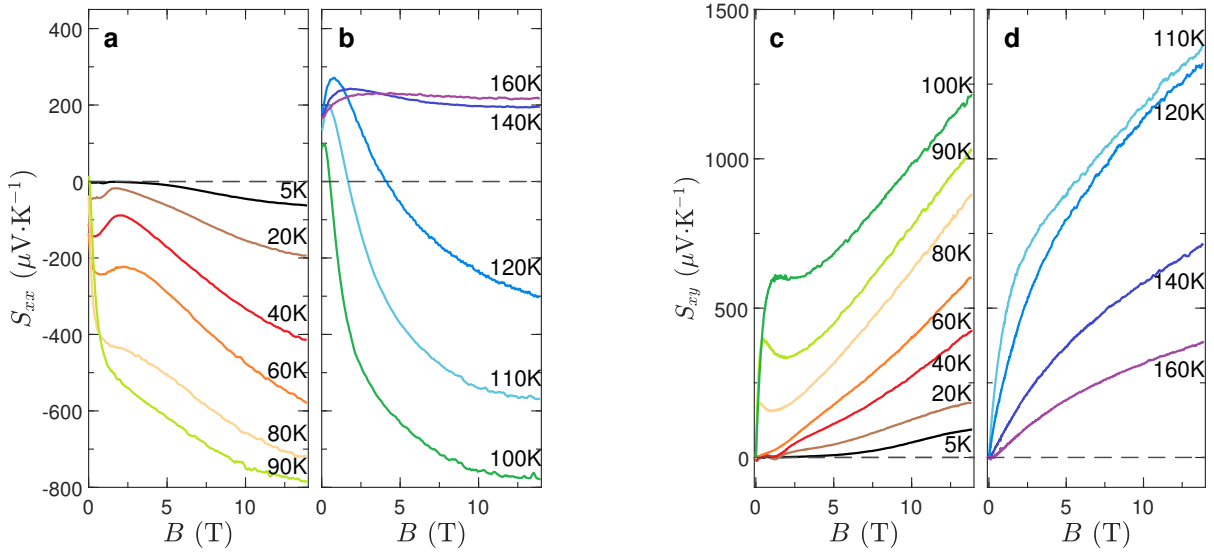


Figure 2: Longitudinal and transverse thermoelectric coefficients as a function of the magnetic field at different temperatures. **a** S_{xx} at $T \leq 90$ K, where the sign of S_{xx} is negative at $B = 0$, and **b** S_{xx} at $T > 90$ K, where the sign is positive at $B = 0$. **c**, **d** show S_{xy} at $T \leq 90$ K and $T > 90$ K, respectively.

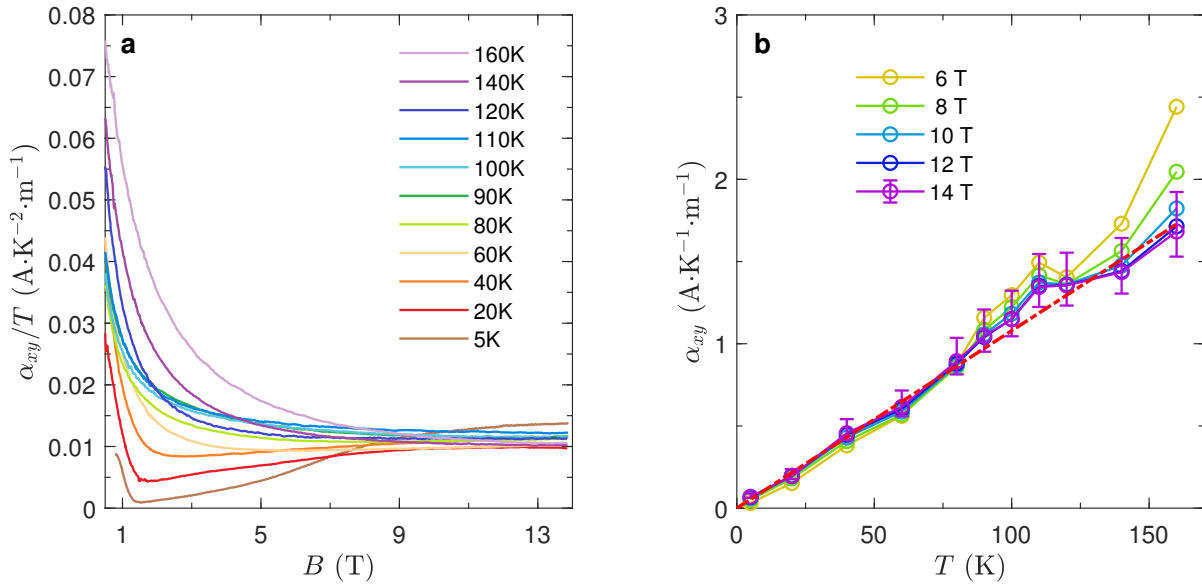


Figure 3: Transverse thermoelectric conductivity. **a** α_{xy}/T as a function of B at different temperatures. α_{xy} is independent of B at high fields. **b** α_{xy} as a function of temperature at different fields. The red dashed line is a guide to the eye. The error bars indicate one standard error, and reflect uncertainties in the measurements of the temperature difference and sample dimensions (see Supplementary Note 1 for detail). For visual clarity, only the error bars for $B = 14$ T are shown.

Supplementary Information for “Observation of a thermoelectric Hall plateau in the extreme quantum limit”

Wenjie Zhang,^{1,*} Peipei Wang,^{2,*} Brian Skinner,^{3,4,*} Ran Bi,¹ Vladyslav Kozii,^{3,5,6} Chang-Woo Cho,²
Ruidan Zhong,⁷ John Schneeloch,⁷ Dapeng Yu,² Genda Gu,⁷ Liang Fu,^{3,†} Xiaosong Wu,^{1,8,†} and
Liyuan Zhang^{2,†}

¹*State Key Laboratory for Artificial Microstructure and Mesoscopic Physics,*

Beijing Key Laboratory of Quantum Devices,

Peking University, Beijing 100871, China

²*Department of Physics, Southern University of Science*

and Technology of China, Shenzhen 518055, China

³*Department of Physics, Massachusetts Institute of Technology, Cambridge, MA 02139, USA*

⁴*Department of Physics, Ohio State University, Columbus, OH 43210, USA*

⁵*Department of Physics, University of California, Berkeley, CA 94720, USA*

⁶*Materials Sciences Division, Lawrence Berkeley National Laboratory, Berkeley, CA 94720, USA*

⁷*Condensed Matter Physics and Materials Science Department,*

Brookhaven National Laboratory, Upton, New York 11973, USA

⁸*Frontiers Science Center for Nano-optoelectronics and Collaborative Innovation Center,*

of Quantum Matter, Peking University, Beijing 100871, China

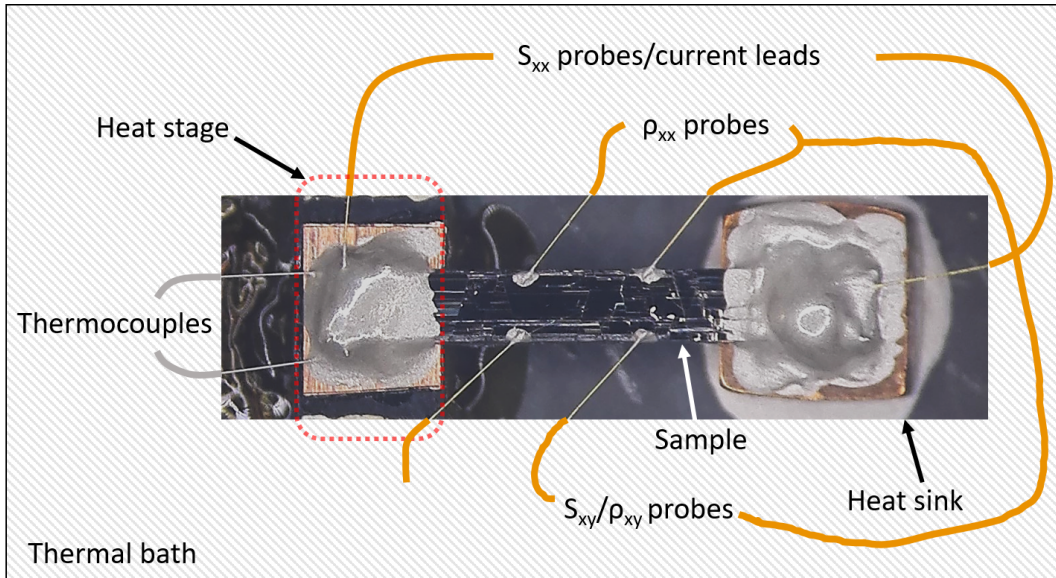
* These authors contributed equally.

† Corresponding Author. E-mail: liangfu@mit.edu (L.F.),

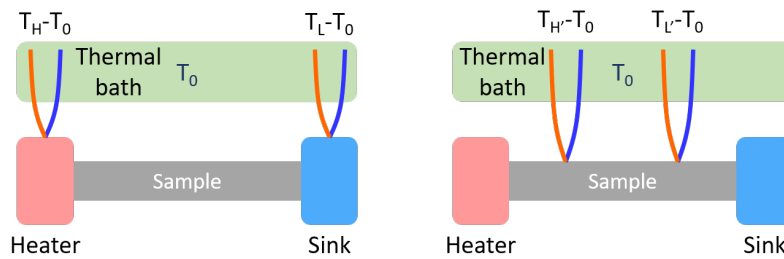
xswu@pku.edu.cn (X.W.),

zhangly@sustc.edu.cn (L.Z.)

SUPPLEMENTARY NOTE 1: EXPERIMENTAL DETAILS



SUPPLEMENTARY FIG. 1: Optical image of our experimental setup. A chip heater (outlined by red dashed line) and a copper heat sink are mounted on the thermal bath by varnish and silver paste, respectively. A copper film is deposited on top of the heater to reduce temperature non-uniformity. Silver paste is used to make electrical contacts. 25 μm gold wires are used for electrical leads due to their small Seebeck coefficient. A Type-E thermocouple measures the temperature difference between the hot end of sample and the thermal bath, with one joint attaching to the sample and the other attaching to the pad on the thermal bath.



SUPPLEMENTARY FIG. 2: Schematics of two-point measurement (left) and four-point measurement (right) setups.

The optical image of our measurement setup is shown in Supplementary Fig. 1. We use a two-point method to measure the temperature difference between the hot end and cold end of

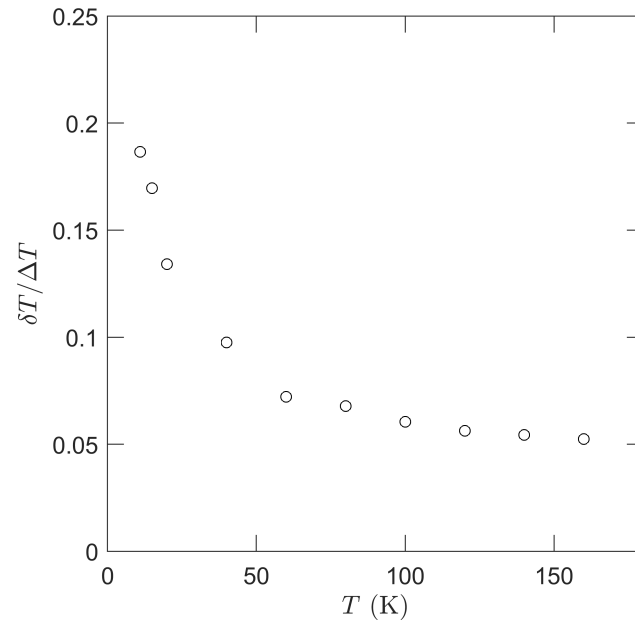
the sample (see Supplementary Fig. 2, left). Normally, two Type-E thermocouples are attached to the heater stage and the heat sink, respectively. The differential of the measured values between two stages is $\Delta T = (T_H - T_0) - (T_L - T_0) = T_H - T_L$. Here, T_H , T_L and T_0 are the temperature of the hot end, the heat sink and the thermal bath, respectively. In our experiment, only one thermocouple is used to get $T_H - T_0$, as the measured $T_L - T_0$ is found to be at most 3% of $T_H - T_0$ due to the good thermal contact between the copper sink and the thermal bath, meaning $\Delta T \approx (T_H - T_0)$. Thermoelectric voltages are measured through gold wires attached to two ends of the sample and the voltage probes in the middle. ρ_{xx} and ρ_{xy} are measured by a standard four-point method.

In general, there are two main types of thermoelectric measurement setups, i.e., two-point and four-point methods, shown in Supplementary Fig. 2. In a two-point setup, a sample is mounted such that it bridges a high temperature stage and a low temperature one. Thermometers are attached to the stages and measure the temperature difference ΔT between the two stages, while electric contacts attached to two ends of the sample are used to measure the thermoelectric voltage V . Since there is contact thermal resistance between the sample and the stages, and hence a temperature difference, the actual ΔT is smaller than the measured one, resulting in underestimation of the thermoelectric ratio $V/\Delta T$. So, it is important to make good thermal contacts so that the contact thermal resistance is much smaller than the thermal resistance of the sample. A four-point method mitigates this problem by attaching thermometers directly to the sample. In such a case, the thermal contacts between the sample and the stages become irrelevant. However, this four-point method works only if the thermal resistance of the thermometer connection is much higher than both that of the sample and the contact thermal resistance between thermometers and the sample. If the former condition is not met, significant heat current will be drawn through the thermometers. This heat leakage gives rise to a non-uniform temperature gradient across the sample, affecting the calculation of the Nernst effect. If the latter condition is broken, the measured ΔT is smaller than the actual one, leading to an overestimation of the thermoelectric coefficients: the so-called cold finger effect.

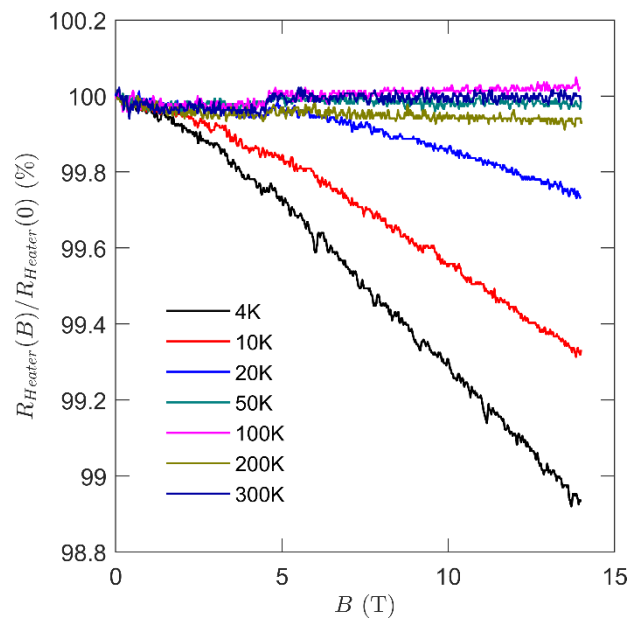
ZrTe₅ is a van der Waals layered material. Moreover, in each layer, there are Zr-Te chains running along the a direction, while the interchain bonding is relatively weak, making it quasi-1D material. As a result, single crystals of ZrTe₅ are in the shape of a whisker or thin ribbon. Due to

the weak van der Waals interlayer coupling, crystals are soft and readily peeled off. These geometric and mechanical characteristics makes our thermoelectric measurements non-trivial. Furthermore, the thermal conductivity of ZrTe₅ is relatively low, which, in combination with small cross-section of the sample, leads to a large thermal resistance. Consequently, it can be challenging to satisfy the condition for the four-point method. For this reason, a two-point method is preferable, especially when the sample is small [1]. As the sample is a ribbon, a large contact area between the sample and the stages, relative to the cross-section area of the sample, can be readily achieved. By further applying abundant silver paste, the contact thermal resistance can be made small. We have measured the temperature difference between one end of the sample and the thermal bath by attaching a thermocouple to that end. As shown in Supplementary Fig. 3, the difference is less than 10% of the measured ΔT above 40 K. This is not significant in a thermoelectric measurement. However, at low temperatures, it can amount to 18%. Consequently, the low temperature thermoelectric coefficients may be appreciably larger than the measured ones.

Let us now quantitatively estimate the heat leakage through the thermometers in a four-point method using the dimensions of our setup. The separation between the heater and heat sink is 1.35 mm. The cross-section of sample #1, presented in the main text, has an area 0.36 mm by 0.25 mm. The thermal conductivity of ZrTe₅ is about 7-20 W/m·K in the temperature range of this study, according to previous reports [2]. The thermal conductivity reported by Constantan and Chromel, which, to the best of our knowledge, is only available at temperatures down to 100 K, are 19W/m·K and 13W/m·K at 100 K, respectively [3]. The thermocouples we used have a diameter of 25 μm with a length of about 3 mm limited by the chip carrier, on which the whole setup is mounted. Neglecting the unknown contact thermal resistance of the thermocouples and using the Fourier's law $JQ = -\kappa\nabla T$, the heat leakage through thermocouple wires is about 0.8 – 1.0% of the total heat through the sample at 100 -150 K. So, for this sample, the heat leakage is not a problem. However, for sample #2, presented in the Supplementary Information, the cross-section is only 0.25 mm by 0.04 mm, and the ratio reaches 7 - 9%.

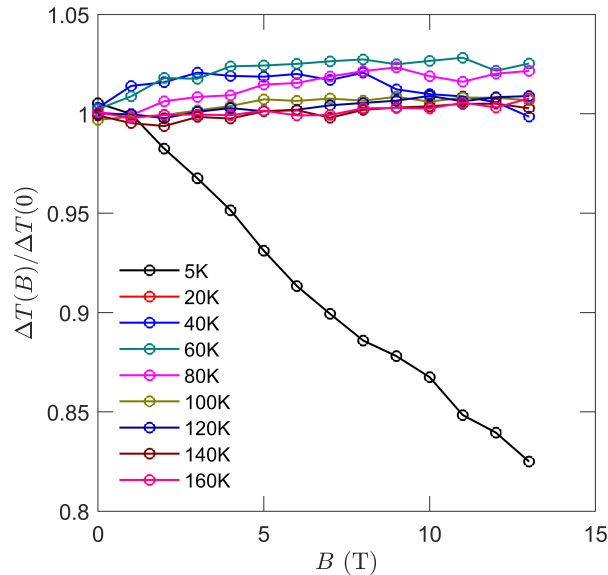


SUPPLEMENTARY FIG. 3: Estimation of the upper bound for the error of the measured temperature difference due to the contact thermal resistance between the cold end of the sample and the thermal bath. ΔT is the measured temperature difference between the hot end of the sample and the thermal bath, which is used to calculate the thermoelectric coefficients, while δT is the measured temperature difference between the cold end of the sample and the thermal bath. Above 50 K, the error is about 5%, but it increases to 18% at low temperature.



SUPPLEMENTARY FIG. 4: Magnetoresistance of the heater.

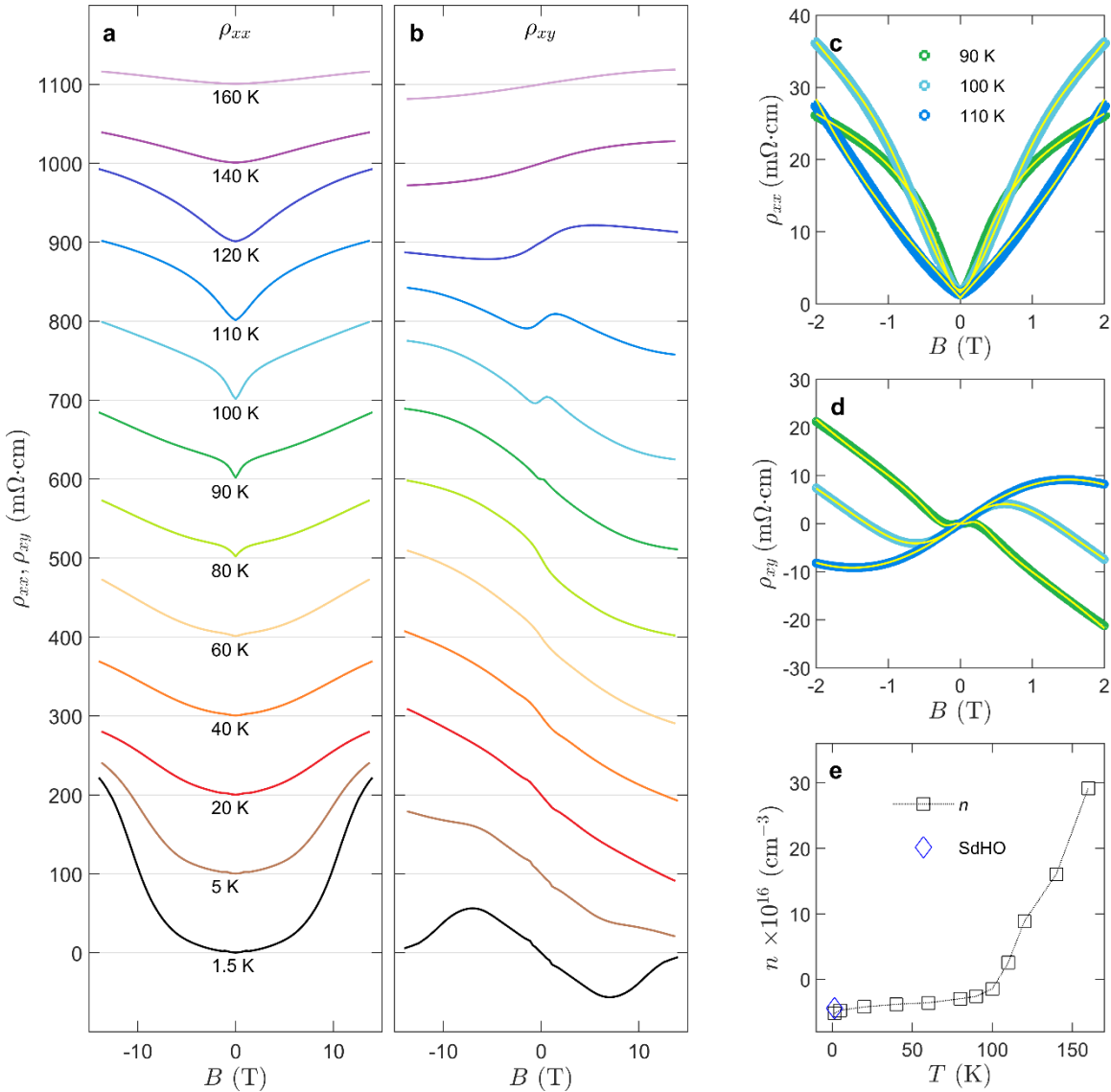
When applying a high magnetic field, the characteristics of thermometers may change. Care needs to be taken to obtain the correct ΔT . In this experiment, we used a Type-E thermocouple, which is field-independent above 20 K, although it gains some dependence below this temperature. To circumvent this issue, we adopted a strategy to make sure that ΔT is field independent so that there is no need to measure it in field. Since the heater resistance barely changes with field, as shown in Supplementary Fig. 4, the heating power remains unchanged under a constant current. Therefore, the key of the strategy is to make sure that the thermal resistance between two stages is much smaller than that of the sample. In this case ΔT does not vary with the latter. To achieve this requirement, the heater, consisting of a meandering thin metal strip on a 500 μm thick alumina substrate, is directly mounted on the thermal bath, using silver paste or varnish. On top of the heater, a thick copper film is deposited to ensure a uniform temperature on the stage. With this design, a heating power of 2.5– 8.1 mW was required to produce $\Delta T \sim 91 - 257$ mK. The heat current through the sample is estimated as 12-53 μW , using the available thermal conductivity of ZrTe_5 [2] and the geometry of the sample. Apparently, only at most 1.5 % of the total heat current goes through the sample, which can have little effect on ΔT . The thermal conductance of alumina is unlikely to have any field dependence. In fact, above 20 K, where our thermocouple is field-independent, ΔT was found to be fairly constant in fields, as seen in Supplementary Fig. 5.



SUPPLEMENTARY FIG. 5: Field dependence of the thermoelectric signal of a thermocouple measuring the temperature difference between the heat stage and the thermal bath.

Under an applied magnetic field, the Nernst effect appears, which in this experiment is measured adiabatically. Under this condition, the Righi-Leduc effect generates a transverse temperature gradient, which in turn contributes a transverse electric field. This additional field has to be taken into account when obtaining the isothermal Nernst coefficient, which is used to calculate the thermoelectric Hall conductivity α_{xy} in this work. The Righi-Leduc effect is usually small. When the thermal conductivity of the material is dominated by the lattice contribution, the transverse temperature gradient is negligible. Then, the adiabatic Nernst coefficient is equivalent to the isothermal one [4]. This is in fact the case in ZrTe₅. The thermal conductivity of ZrTe₅ single crystals is about, 7 – 20 W/m·K according to previous reports [2]. Using the measured resistivity of our sample, we can estimate the electronic contribution to the thermal conductivity, based on the Wiedemann-Franz law, $\kappa/\sigma = LT$. It turns out to be $\sim 0.05 - 0.7$ W/m·K, only 3% of the total thermal conductivity. Therefore, our measurements directly produce the isothermal Nernst coefficient.

SUPPLEMENTARY NOTE 2: ANALYSIS OF MAGNETORESISTANCE



SUPPLEMENTARY FIG. 6: Electrical transport measurements. **a, b** Longitudinal electrical resistivity ρ_{xx} and transverse electrical (Hall) resistivity ρ_{xy} versus the magnetic field at different temperatures. Curves are shifted for clarity. **c, d** ρ_{xx} and ρ_{xy} at 90 K, 100 K, 110 K for $B < 2$ T. Bright solid lines are fits to a two band model. **e** Carrier densities as a function of temperature. Positive values represent holes, while negative values represent electrons. The diamond symbol represents the carrier density calculated from Shubnikov-de Haas oscillations at 1.5 K.

Supplementary Fig. 6 shows the magnetoresistance and the Hall resistance of the sample presented in the main text. The resistivity strongly increases with field, e.g., by two to three orders of magnitude at $B = 14$ T. Such a large magnetoresistance is typical for Dirac semimetals

[5]. At low temperatures, the Hall resistivity is rather linear below 6 T, indicating single band conduction. The linearity persists deep into the quantum limit. However, a strong deviation appears above 6 T. We believe that such a nonlinear Hall voltage in the extreme quantum limit is the result of two-carrier contributions, as expected when the Fermi level shifts towards the Dirac point with increasing magnetic field. This shifting of the Fermi level is precisely the mechanism that gives rise to the non-saturating thermopower and transverse thermoelectric conductivity plateau, which are the main focus of this work. The low-field slope of ρ_{xy} shows a sign-reversal at about 90 K, indicating the change of carrier from electron to hole, as expected by the Lifshitz transition in this material.

At temperatures that are much lower or much higher than 90 K, the Fermi level is not so close to the Dirac point and the transport is more or less one-carrier dominated at low fields. Correspondingly, the low-field Hall resistivity is relatively linear and the carrier density can be simply calculated from the Hall slope. On the other hand, around 90 K, where the Fermi level is in the vicinity of the Dirac point, a significant number of electrons and holes are thermally excited. The existence of two types of carriers with comparable densities causes ρ_{xy} to become non-linear even at relatively low fields. Consequently, a two-carrier model such that $\hat{\rho}_{tot}^{-1} = \hat{\rho}_e^{-1} + \hat{\rho}_h^{-1}$, is necessary to describe the magnetotransport and extract the carrier density. Here $\hat{\rho}_{tot}$, $\hat{\rho}_e$ and $\hat{\rho}_h$ are the resistivity tensors of the total, electron contribution and hole contribution, respectively. For the longitudinal component of the resistivity tensor, ρ_{xx} , we need to take into account the strong magnetoresistance that a Dirac semimetal often exhibits. The following generic expressions are used to describe both the electron and hole transport,

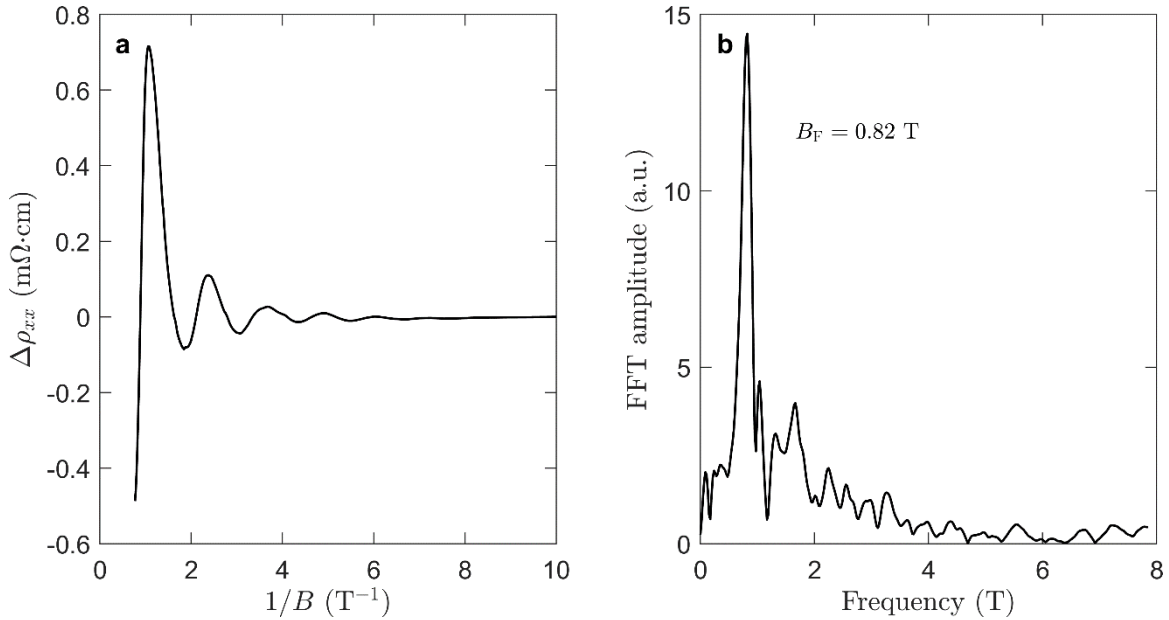
$$\begin{cases} \rho_{xx}(B) = \rho_0 + a|B| + bB^2 \\ \rho_{xy}(B) = R_H B \end{cases}, \hat{\rho} = \begin{pmatrix} \rho_{xx} & \rho_{xy} \\ -\rho_{xy} & \rho_{xx} \end{pmatrix} \quad (2-1)$$

By fitting data around 90 K, the carrier densities of holes and electrons, n_h and n_e , are obtained. Their difference, $n_h - n_e$, which reflects the Fermi level, is plotted in Supplementary Fig. 6e. The full results for n_h , n_e , μ_h , and μ_e are shown in Table 1. The temperature dependence of the carrier density is consistent with the Lifshitz transition observed in the angle resolve photo-emission spectroscopic study [6]. Overall, the mobility decreases with temperature, except for some deviation around 100 K. This is because a two-band model has to be used in this regime and increase in the number of fitting parameters leads to larger uncertainty.

Temperature (K)	1.5	5	20	40	60	80	90	100	110	120	140	160
n_h (10^{16} cm^{-3})	-	-	-	-	-	-	1.8	5.3	5.3	8.8	16.1	29.2
n_e (10^{16} cm^{-3})	5.2	4.7	4.2	3.8	3.6	3.0	4.4	6.8	2.8	-	-	-
μ_h ($\text{m}^2\text{V}^{-1}\text{s}^{-1}$)	-	-	-	-	-	-	5.7	7.3	14.6	7.2	5.0	3.5
μ_e ($\text{m}^2\text{V}^{-1}\text{s}^{-1}$)	42.9	64.0	55.3	35.8	16.9	10.2	4.9	0.1	0.2	-	-	-

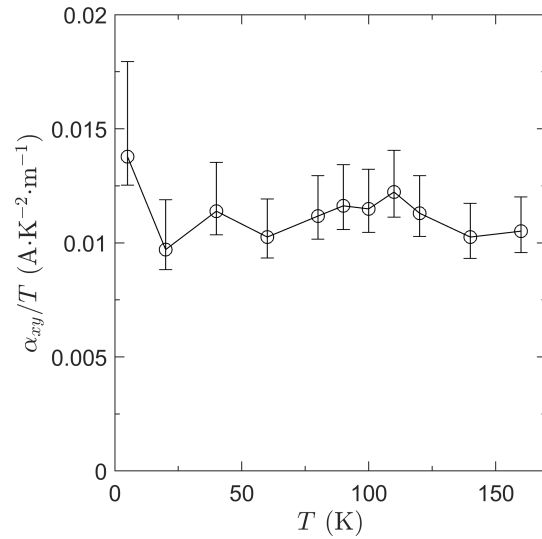
SUPPLEMENTARY TABLE 1: Carrier density and mobility.

Supplementary Fig. 7 shows the oscillatory part of the magnetoresistance at 1.5 K, which is periodic in $1/B$. At least six periods of oscillations can be identified. The FFT spectrum displays a sharp peak at about 0.82 T, which agrees well with the slope of the Landau plot shown in Fig. 1 of the main text. From the oscillation frequency, we estimate the carrier density $4.3 \times 10^{16} \text{ cm}^{-3}$.

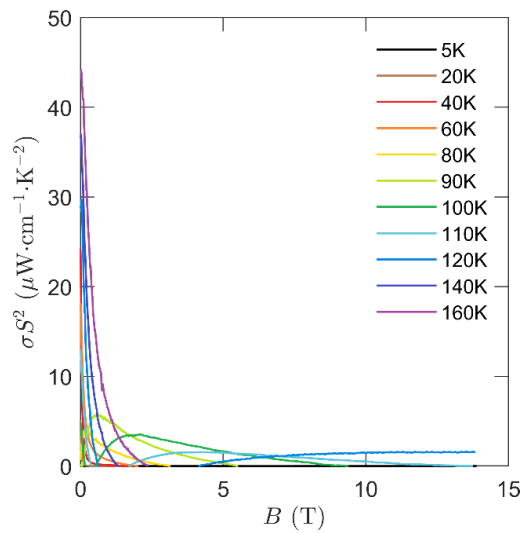


SUPPLEMENTARY FIG. 7: Quantum oscillations of magnetoresistance at 1.5 K. **a** Oscillations of the magnetoresistance after subtraction of a background. **b** Fast Fourier transformation analysis of the quantum oscillation.

SUPPLEMENTARY NOTE 3: ANALYSIS OF THERMOELECTRIC PROPERTIES

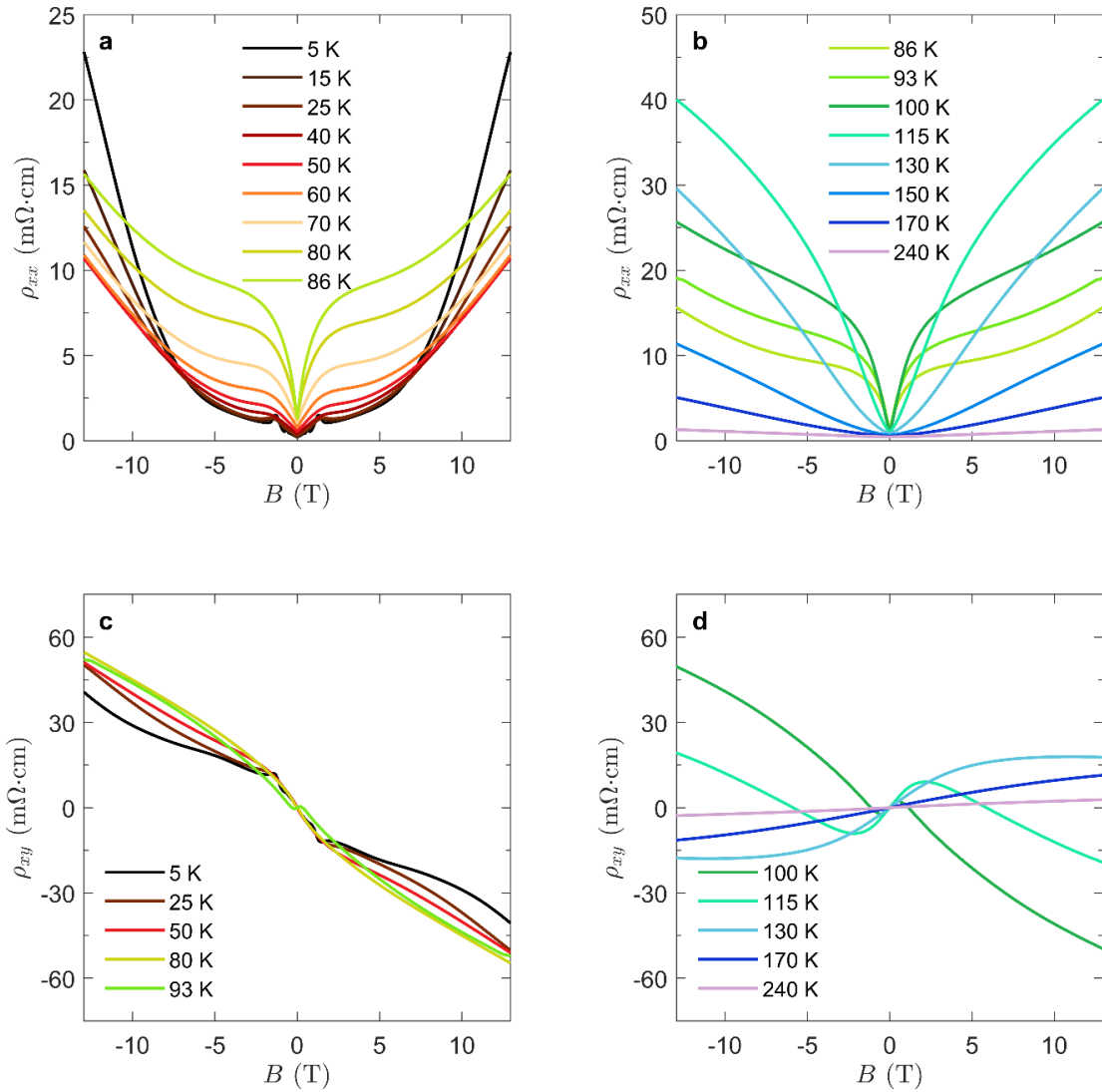


SUPPLEMENTARY FIG. 8: Thermoelectric conductivity α_{xy}/T at 14 T for different temperatures. The lowest temperature point shows a larger deviation. The error bars reflect uncertainties in measurements of the temperature difference and sample dimensions, and indicate one standard error. The uncertainty in the temperature difference is estimated from the plot in Supplementary Fig. 3.

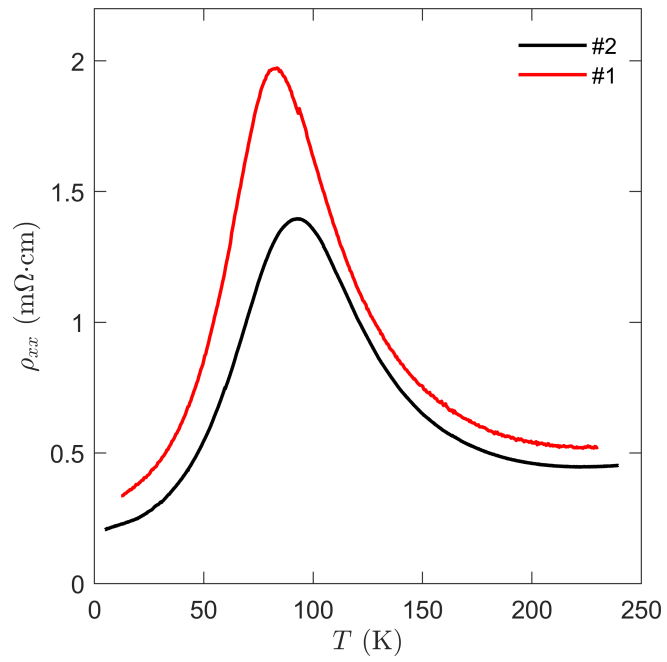


SUPPLEMENTARY FIG. 9: Power factor as a function of magnetic field. Overall, it decreases with increasing field. Due to the sign change of the Seebeck coefficient, the curves around 90 K are non-monotonic.

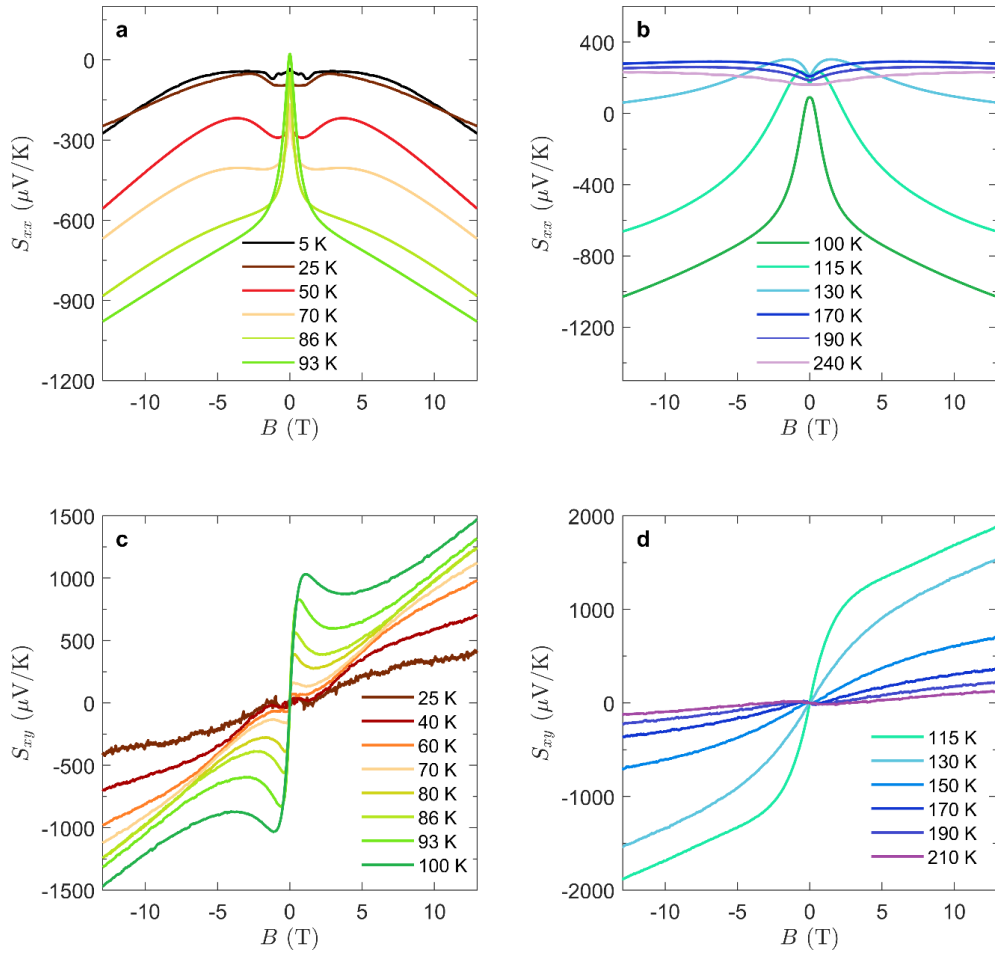
SUPPLEMENTARY NOTE 4: DATA FROM AN ADDITIONAL SAMPLE



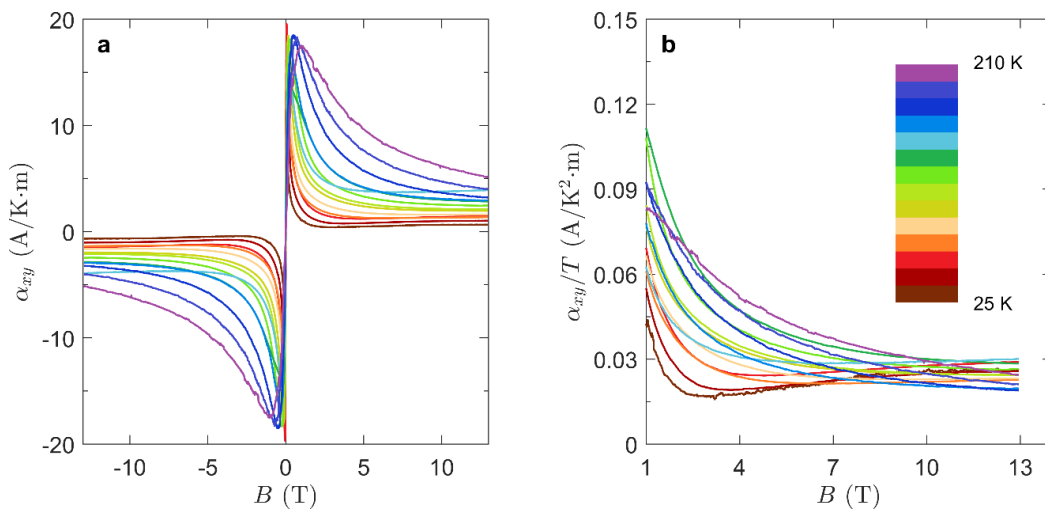
SUPPLEMENTARY FIG. 10: Electrical transport properties of sample #2. **a, b** Longitudinal electrical resistivity ρ_{xx} at different temperatures, showing strong magnetoresistance. At low temperatures, quantum oscillations appear at low fields. **c, d** Transverse electrical (Hall) resistivity ρ_{xy} . When the temperature is low, ρ_{xy} is linear in B , suggesting a single band. ρ_{xy} deviates from the linear dependence when the system is in the quantum limit. Around 100 K, the Hall resistivity becomes nonlinear, implying two-band transport.



SUPPLEMENTARY FIG. 11: The zero-field resistivity ρ_{xx} as a function of temperature for sample #2 (lower, black curve) as compared to sample #1 (upper, red curve).



SUPPLEMENTARY FIG. 12: Thermoelectric coefficients of sample #2. **a, b** S_{xx} at different temperatures. **c, d** S_{xy} .



SUPPLEMENTARY FIG. 13 Transverse thermoelectric conductivity of sample #2. **a**, α_{xy} as a function of B at different temperatures. **b**, Plateau of α_{xy}/T at high magnetic field.

Supplementary Figs. 10-13 show data taken from another sample, which we dub sample #2. Overall, the results are very similar to the sample (“sample #1”) presented in the main text. The temperature dependence of the longitudinal electrical resistivity has a maximum at about 93 K. At 1.5 K, the sample mobility is about $370,000 \text{ cm}^2\text{V}^{-1}\text{s}^{-1}$. In the field dependence of the resistivity, quantum oscillations are well developed at low magnetic fields. The quantum limit is reached above 2 T, slightly higher than for the sample in the main text, suggesting a slightly larger value of the electron concentration at $B=0$. ρ_{xy} is linearly dependent on B below the quantum limit at low temperatures, while it becomes nonlinear around the temperature of the resistivity maximum. These features are consistent with the Lifshitz transition discussed in the main text. One can notice that the magnetoresistance effect is somewhat weaker in sample #2 as compared to sample #1, particularly at high fields ~ 10 T. In our samples, one of the primary drivers of magnetoresistance at such high fields is the variation in carrier concentration with field arising from the Lifshitz transition. In sample #2 achieving a large variation seems to require a relatively higher value of magnetic field as compared to sample #1, which is consistent with the sample #2’s larger electron concentration at $B = 0$.

Supplementary Fig. 12 shows the thermoelectric coefficients, S_{xx} and S_{xy} . The results in the main text are reproduced in this sample. Both coefficients exhibit a mostly linear increase in the quantum limit, with S_{xy} becoming as large as $1900 \mu\text{V}/\text{K}$. Supplementary Fig. 13 shows the transverse thermoelectric conductivity. The value of α_{xy}/T at different temperatures converges to a plateau value in the range $0.02 - 0.03 \text{ A}/\text{K}^2\cdot\text{m}$ at high magnetic field. Although this value is higher than the one in the main text, it is still in reasonably good agreement with the theory. The difference between samples may be explained by variation of the Fermi velocity among samples due to high sensitivity of the band structure on the lattice constant, or by slight differences in alignment with the magnetic field (note that ZrTe_5 has a strongly anisotropic Fermi velocity). We reiterate that the variation of the band structure of ZrTe_5 is manifested in many experiments with various techniques [7], with three different topological phases being reported. Thinning the thickness of a crystal down to 180 nm can increase the band gap from zero to 10 meV, even though no quantum confinement is expected at this thickness [8]. The peak in the temperature dependence of the resistivity, one of the characteristic features of ZrTe_5 , can vary from 0 to 140 K. Therefore, it is not surprising that the Fermi velocity may vary from sample to sample. Additionally, the apparent deviation from the universal plateau value at low

temperatures may be related to the presence of a small band gap, as we discuss theoretically in Sec. VI.

SUPPLEMENTARY NOTE 5: DISCUSSION OF POSSIBLE PHONON DRAG EFFECTS

The expression for α_{xy} presented in the main text, Eq. (1), is derived under the assumption that there is no significant phonon contribution to the thermoelectric conductivity. Here we discuss the possible role of phonons. In particular, we discuss whether phonon drag effects may be responsible for the slight upturn in α_{xy} that is suggested by Fig. 3a and Supplementary Fig. 11b with increasing field at the lowest temperatures.

While phonon modes are typically electroneutral, and have no direct coupling to magnetic field, they may still contribute to α_{xy} through the phonon drag effect: when an electric current is present, electron-phonon scattering processes give the phonon system a net drift velocity. Thus, an electron heat current may be accompanied by a collinear phonon heat current. Such a phonon current would tend to increase the thermoelectric conductivity.

One can make an upper-bound estimate for the effect of phonon drag by assuming that the phonon drift velocity is identical to the electron drift velocity. This strongest-case scenario corresponds to the limit of strong electron-phonon scattering and weak phonon-phonon or phonon-impurity scattering. [9] As explained in the main text, the heat current at large magnetic field is directly proportional to the entropy density. Thus, in this same limit the contribution of phonon drag effects to α_{xy} is directly proportional to the phonon entropy. In the limit of low temperature the phonon entropy is dominated by acoustic phonons, which have an entropy

$$S_{ph} \sim \frac{k_B^4 T^3}{\hbar^3 v_s^3} \sim \frac{k_B}{V_0} \left(\frac{T}{\theta_D} \right)^3 \quad (5-1)$$

per unit volume, where v_s is the speed of sound, V_0 is the unit cell volume, and θ_D is the Debye temperature. As discussed in the main text, the electron entropy in the EQL is of order

$$S_{el} \sim \frac{N_f k_B^2 T e B}{\hbar^3 v_F}. \quad (5-2)$$

Thus, at low temperatures and in the EQL the relative contribution of phonon drag to α_{xy} can be no larger than

$$\left(\frac{\alpha_{xy}^{(\text{phonon drag})}}{\alpha_{xy}^{(\text{electrons})}} \right) < \frac{S_{ph}}{S_{el}} \sim \frac{\hbar^2 v_F}{N_f k_B T V_0 e B} \left(\frac{T}{\theta_D} \right)^3. \quad (5-3)$$

For ZrTe₅ the Debye temperature $\theta_D \approx 150$ K [10] and the unit cell volume $V_0 \approx 400 \text{ \AA}^3$.

While this estimate for $\alpha_{xy}^{(\text{phonon drag})} / \alpha_{xy}^{(\text{electrons})}$ gives a numerical value as large as several tenths within the EQL, it predicts a temperature and field dependence that is inconsistent with our observations. In particular, Supplementary Eq. (5-3) suggests that the contribution of phonon drag is larger at higher temperatures and at lower fields. On the other hand, the slight deviation from the plateau value of α_{xy} becomes more pronounced in the opposite limit of lower temperatures and at higher fields. Thus, we find it more likely that the slight deviation in α_{xy} from the plateau value is associated with the presence of a very small gap. We discuss this possibility and its consequences in the following section.

SUPPLEMENTARY NOTE 6: THEORETICAL CALCULATION OF α_{xy} FOR THE CASE OF A MASSIVE DIRAC DISPERSION

In this section we present a theoretical calculation of the thermoelectric Hall conductivity α_{xy} for the case of a massive Dirac dispersion. This analysis is a straightforward generalization of the results obtained in Ref. [11] to the case of a finite band gap.

The energy of a massive Dirac particle in a magnetic field is given by the expression

$$\varepsilon_n(k_z) = \text{sign}(n) \cdot \sqrt{\Delta^2 + 2e\hbar B|n|v_\perp^2 + v_F^2\hbar^2k_z^2} \quad (6-1)$$

where 2Δ is the band gap, v_F is the Fermi velocity in the magnetic field direction z , and v_\perp is the velocity in plane perpendicular to the field direction (more carefully, it is the geometric mean of v_x and v_y). The density of states is then given by

$$\nu(\varepsilon) = \frac{N_f B e}{\pi^2 \hbar^2 v_F} \text{Re} \left(\frac{|\varepsilon|}{2\sqrt{\varepsilon^2 - \Delta^2}} + \sum_{n=1}^{\infty} \frac{|\varepsilon|}{\sqrt{\varepsilon^2 - \Delta^2 - 2\hbar v_\perp^2 e B n}} \right) \quad (6-2)$$

where N_f is the number of Dirac nodes (each of the nodes is double degenerate).

The thermoelectric Hall conductivity is determined by the expression [11]

$$\alpha_{xy} = \frac{e N_f}{\pi \hbar} \sum_{n=0}^{\infty} \int_0^{\infty} \frac{dk_z}{\pi} \left[s \left(\frac{\varepsilon_n(k_z) - \mu}{k_B T} \right) + s \left(\frac{\varepsilon_n(k_z) + \mu}{k_B T} \right) \right] \quad (6-3)$$

where μ is the chemical potential, and T is the temperature. The notation $\sum_{n=0}^{\infty}$ is used to mean that there is an extra factor $1/2$ multiplying the $n = 0$ term of the sum, and $\varepsilon_0(k_z)$ should be understood as $\varepsilon_0(k_z) = \sqrt{\Delta^2 + v_F^2 \hbar^2 k_z^2}$ in the above expression. The entropy per electron state is given by

$$s(x) = -k_B [n_F \ln n_F + (1 - n_F) \ln(1 - n_F)] = k_B \left[\ln(1 + e^x) - \frac{x}{1 + e^{-x}} \right] \quad (6-4)$$

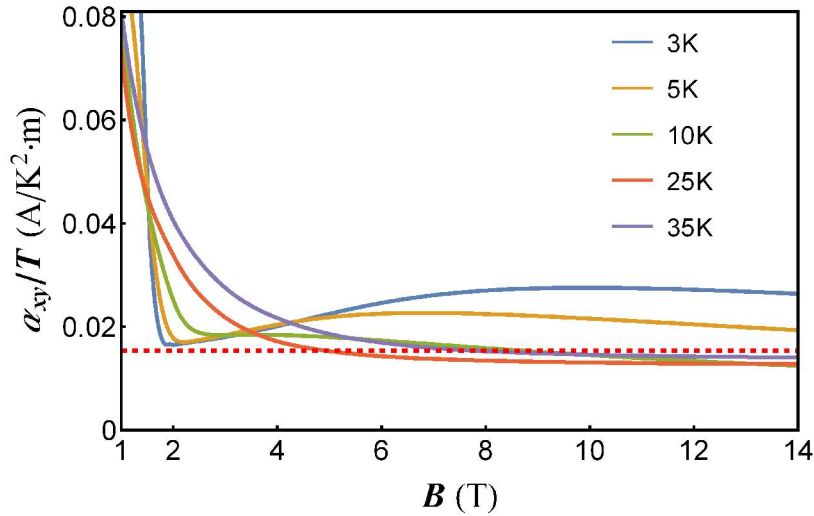
where $n_F(\varepsilon) = [1 + \exp(\varepsilon/k_B T)]^{-1}$ is the Fermi-Dirac distribution.

Finally, the chemical potential μ should be determined self-consistently from the equation

$$\int_0^{\infty} d\varepsilon \nu(\varepsilon) n_F(\varepsilon - \mu) - \int_{-\infty}^0 d\varepsilon \nu(\varepsilon) [1 - n_F(\varepsilon - \mu)] = n_0 \quad (6-5)$$

where n_0 is net electron concentration.

The equations in this section fully determine the thermoelectric Hall conductivity α_{xy} as a function of magnetic field B , temperature T , and electron concentration n_0 . An example of the solution is shown in Supplementary Fig. 14. Note, in particular, that at temperatures much smaller than the band gap and at sufficiently high magnetic fields, the electron dispersion near the Fermi level is essentially that of Schrodinger particles, which do not exhibit a quantized plateau [11].



SUPPLEMENTARY FIG. 14: An example calculation of α_{xy} as a function of B for different temperatures T . This result is obtained as a solution of Supplementary Eqs. (6-1) through (6-5) with $n_0 = 5 \times 10^{16} \text{ cm}^{-3}$, $N_f = 1$, $v_F = 3 \times 10^4 \text{ m/s}$, $v_{\perp} = 6v_F$, and $\Delta/k_B = 30\text{K}$. The red dashed line indicates the position of the plateau for the same parameter values when $\Delta = 0$, i.e., $\alpha_{xy}^{\text{plateau}} = T e k_B^2 N_f / 6 v_F \hbar^2$.

SUPPLEMENTARY REFERENCES

- [1] Bartosz M. Zawilski, Roy T. Littleton IV, and Terry M. Tritt, *Rev. Sci. Instrum.* **72**, 1770 (2001).
- [2] B. M. Zawilski, R. T. Littleton IV, and Terry M. Tritt, *Appl. Phys. Lett.* **77**, 2319 (2000).
- [3] B. Sundqvist, *J. Appl. Phys.* **72.2**, 539 (1992).
- [4] K. Sugihara, *J. Phys. Soc. Jpn.* **27**, 362 (1969).
- [5] T. Liang, Q. Gibson, M. N. Ali, M. Liu, R. J. Cava, and N. P. Ong, *Nature Materials* **14**, 280 (2014).
- [6] Y. Zhang, C. Wang, L. Yu, G. Liu, A. Liang, J. Huang, S. Nie, X. Sun, Y. Zhang, B. Shen, J. Liu, H. Weng, L. Zhao, G. Chen, X. Jia, C. Hu, Y. Ding, W. Zhao, Q. Gao, C. Li, S. He, L. Zhao, F. Zhang, S. Zhang, F. Yang, Z. Wang, Q. Peng, X. Dai, Z. Fang, Z. Xu, C. Chen, and X. J. Zhou, *Nature Communications* **8**, 15512 (2017).
- [7] P. Shahi, D. J. Singh, J. P. Sun, L. X. Zhao, G. F. Chen, Y. Y. Lu, J. Li, J.-Q. Yan, D. G. Mandrus, and J.-G. Cheng, *Phys. Rev. X* **8**, 021055 (2018).
- [8] Zhi-Guo Chen, R. Y. Chen, R. D. Zhong, John Schneeloch, C. Zhang, Y. Huang, Fanming Qu, Rui Yu, Q. Li, G. D. Gu, and N. L. Wang, *PNAS* **114**, 816 (2017).
- [9] J. M. Ziman, *Principles of the Theory of Solids*, Cambridge University Press, 1972.
- [10] Jie Zhu, Tianli Feng, Scott Mills, Peipei Wang, Xuewang Wu, Liyuan Zhang, Sokrates T. Pantelides, Xu Du, Xiaojia Wang, *ACS Appl. Mater. Interfaces* **10**, 40740 (2018).
- [11] V. Kozii, B. Skinner, and L. Fu, *Phys. Rev. B* **99**, 155123 (2019).